



Hybrid 0D/2D edamame shaped ZnIn_2S_4 photoanode modified by Co-Pi and Pt for charge management towards efficient photoelectrochemical water splitting

Miao Zhou^a, Zhihua Liu^a, Qinggong Song^b, Xifei Li^c, Bowen Chen^a, Zhifeng Liu^{a,*}

^a School of Materials Science and Engineering, Tianjin Chengjian University, 300384, Tianjin, China

^b College of Science, Civil Aviation University of China, Tianjin, 300300, China

^c Institute of Advanced Electrochemical Energy & School of Materials Science and Engineering, Xi'an University of Technology, Xi'an, 710048, China

ARTICLE INFO

Keywords:

Edamame
 ZnIn_2S_4
Photoanode
Photoelectrochemical performance
Cocatalysts

ABSTRACT

Charge separation and transport as well as light absorption are pivotal in determining the efficiency of solar water splitting devices. Herein, we have designed a novel edamame shaped ZnIn_2S_4 nanostructures consisted of hybridized nanoflakes (2D) and nanoparticles (0D) on ITO conductive substrate through a simple hydrothermal method for PEC water splitting for the first time. The growth mechanism of 0D/2D ZnIn_2S_4 is proposed and discussed in detail. The series of PEC measurements indicate that edamame shaped 0D/2D ZnIn_2S_4 films exhibit relatively higher PEC activity ($0.37 \text{ mA}/\text{cm}^2$ at 1.23 V vs. RHE) than that of ZnIn_2S_4 NFs and ZnIn_2S_4 NPs due to the enhanced light absorption and efficient charge separation and transfer and increased active sites. Additionally, after selectively depositing Co-Pi cocatalyst and Pt NPs on the top and bottom sides of edamame shaped ZnIn_2S_4 photoanodes, charge recombination at the surface and interface can be efficiently reduced. The spatial Co-Pi cocatalyst drives holes to flow to the surface, while the Pt NPs facilitate the electrons in the opposite directions. Thus, the integrated Co-Pi/ ZnIn_2S_4 /Pt equipment without any additional doping presents an increased photocurrent density with $0.91 \text{ mA}/\text{cm}^2$ at 1.23 V vs. RHE. This work highlights that edamame shaped ZnIn_2S_4 can be a promising candidate for photoelectrochemical behavior and route such as coupling of Co-Pi and Pt co-catalysts on photoanodes have an interfacial electric field can provide a new avenues to design efficient PEC devices in future.

1. Introduction

Solar driven photoelectrochemical (PEC) water splitting for hydrogen production over semiconductor photocatalysis has been identified as an attractive and sustainable strategies to meet the growing demand of global energy and ensure a sustainable energy supply for the future [1–3]. The discovery of water splitting over titanium dioxide (TiO_2) by Honda and Fujishima in the early 1970s ignited vast interest in PEC water splitting [4,5]. Quickly after that, it was first proposed that the power conversion efficiency (PCE) for the semiconductor-based solar water splitting with a single junction cell can be up to 30.7% [6,7]. To this end, continuous efforts have been made to maximize the energy conversion efficiency, but the reported efficiency can only reach 12.4% which is only about half of the theoretical efficiency limit for such devices [8]. A key challenge for the sluggish progress is the lack of suitable semiconductor materials, which can absorb broad visible light, be efficient in separating and transporting charge from the bulk

photoelectrode to the surface, and be effective in consuming photo-induced carriers for the surface reaction with minimum overpotential. However, to date, although more than 130 types of semiconductor materials have been used as photoelectrodes [9], no single one can satisfy all the aforesaid requirements.

Aiming to realize high energy conversion efficiency, three general strategies have been pursued and designed energetically. One is to find a new potential compound that has a good balance among various properties of solar water splitting as demonstrated by $\text{CaBi}_6\text{O}_{10}$ [10], BiVO_4 [11], CuWO_4 [12] and others. The second way is to introduce morphology into the fabrication of photoelectrodes. Specific morphology of photoelectrode materials will offer some promise to overcome major shortcomings of them without changing composition. For example, Hong and his coworkers have prepared flower-like $\text{Cu}_2\text{In}_2\text{ZnS}_5$ nanosheets with the highest photocurrent density in contrast to others, due to the enhanced light harvesting and utilizing caused by the uniform morphology of nanosheet [13]. The third

* Corresponding author.

E-mail address: tjulzf@163.com (Z. Liu).

<https://doi.org/10.1016/j.apcatb.2018.11.031>

Received 26 July 2018; Received in revised form 29 October 2018; Accepted 13 November 2018

Available online 16 November 2018

0926-3373/© 2018 Elsevier B.V. All rights reserved.

strategy is to design compound such as heterojunction structure and integrating cocatalysts, a type of semiconductor material composed of mutually complementary multiple components, having a combination of properties not available in one-component material [14,15]. For instance, Liu et al have constructed an all metal oxides $\text{WO}_3/\text{Cu}_2\text{O}$ heterojunction photoelectrode to realize wide light-absorption range [16]. Ye and his groups reported that FeOOH nanospikes modified $\alpha\text{-Fe}_2\text{O}_3$ photoanodes showed an improved photocurrent density, owing to a significant cocatalytic effect of FeOOH [17]. Certainly, with the in-depth study of photocatalytic water splitting, selective deposition of spatial separation cocatalysts on semiconductors has been proposed [18–20]. Qin et al designed Pt and CoO_x simultaneously on the inner and outer surface of TiO_2 nanotubes to realize remarkable high photocatalytic efficiency [21].

Zinc indium sulfide (ZnIn_2S_4) as an important member of layered transition-metal chalcogenides (TMCs) has been extensively studied and potential application in various fields such as thermoelectricity, solar cells, photodetectors, photocatalytic degradation and so on [22–25]. Since Lei and his co-workers utilized ZnIn_2S_4 as a visible-light-driven photocatalyst for hydrogen production firstly [26], it caused great interest in preparation of ZnIn_2S_4 to achieve high energy conversion efficiency. In this work, a novel edamame shaped ZnIn_2S_4 structure consisted of hybrid nanoparticles (0D) and nanoflakes (2D) was designed on the indium tin oxide (ITO) substrate via a feasible hydrothermal route and applied in PEC water splitting for the first time. In this 0D/2D combined edamame shaped ZnIn_2S_4 structure, not only the enhanced light capture can be achieved due to the multiple reflection and scattering of light caused by both nanoflakes and nanoparticles, but also the recombination of photoinduced charge carriers can be restrained to some extent because of more active sites provided by both nanoflakes and nanoparticles. Furthermore, we treated edamame shaped ZnIn_2S_4 with spatial separation co-catalyst (outer for Co-Pi and inner for Pt) to achieve remarkable high water splitting efficiency through the spatial electron-hole separation. In this system, Co-Pi cocatalyst drives the holes to the surface, while a Pt layer collects the electrons in the opposite direction, which can effectively decrease the charge recombination at the surface and interface to further improve the whole water splitting efficiency. The resulting Co-Pi/ ZnIn_2S_4 /Pt photoelectrode exhibits improved PEC activity as expected. Otherwise, the charge carrier generation, separation and catalytic processes have been studied by photoelectrochemical techniques, which is imperative in order to understand and engineer better performing photoelectrodes with higher water splitting efficiency.

2. Experimental section

2.1. Preparation of ZnIn_2S_4 nanostructures

The ZnIn_2S_4 nanostructures were in situ grown on ITO glasses directly via one-step hydrothermal route. In this course, Zinc chloride (ZnCl_2), Indium chloride tetrahydrate ($\text{InCl}_3\cdot 4\text{H}_2\text{O}$) and Thioacetamide (CH_3CSNH_2) were used as the precursor for Zinc, indium and sulfur source, respectively, which were of analytical grade and used without further purification. To be specific, ITO conductive substrates were cleaned by continuously ultrasonication in acetone, ethanol and distilled water for 30 min and then dried for use. After that, the ITO substrate was putted into a 25 ml Teflon-lined stainless steel autoclave at an angle of 45° , facing down. Subsequently, 0.2 mmol of ZnCl_2 , 0.4 mmol of $\text{InCl}_3\cdot 4\text{H}_2\text{O}$ and 1.6 mmol of CH_3CSNH_2 (TAA) were dissolved in 20 ml deionized water and the homogeneous precursor solution was acquired until stirring constantly for 30 min. Then, poured into the prepared Teflon-lined stainless steel autoclave. Following, the autoclave was heated at 180°C for different reaction time in an oven and naturally cooled down to room temperature. The resulting samples were washed with alcohol and deionized water for several times, and then to be dried in air naturally. Finally, the pure ZnIn_2S_4 films were

obtained named as ZIS^{-2} . Besides, different precursor concentrations were achieved. For example, 0.1 mmol of ZnCl_2 , 0.2 mmol of $\text{InCl}_3\cdot 4\text{H}_2\text{O}$ and 0.8 mmol of CH_3CSNH_2 (TAA) and another one (0.4 mmol of ZnCl_2 , 0.8 mmol of $\text{InCl}_3\cdot 4\text{H}_2\text{O}$ and 3.2 mmol of CH_3CSNH_2 (TAA)) were dissolved in 20 ml deionized water and then following the above hydrothermal process. Finally the obtained samples labeled as ZIS-1 and ZIS-3 respectively.

2.2. Fabrication of Co-Pi/ ZnIn_2S_4 /Pt composite photoelectrode

In the first step, Pt layer was grown onto the prepared ITO conductive substrate directly via electrochemical deposition in 0.5 mM H_2PtCl_6 electrolyte, using a three-electrode configuration with a ITO conductive substrates acting as working electrode, an Ag/AgCl as reference electrode and a platinum foil as the counter electrode. In this process, a bias of -0.35 V vs Ag/AgCl was applied until 0.075 C of charge had passed, which took about 300 s. After that, the as-obtained samples were cleaned with alcohol and distilled water to remove the impurity ions staying on the surface of the sample and then dried in the air.

In the second step, the produced Pt/ITO was used to synthesize Pt/ ZnIn_2S_4 through the same way in prepare ZnIn_2S_4 film with 0.2 mmol of ZnCl_2 , 0.4 mmol of $\text{InCl}_3\cdot 4\text{H}_2\text{O}$ and 1.6 mmol of CH_3CSNH_2 (TAA) as precursor solution.

Finally, the Co-Pi co-catalyst was loaded onto the surface of Pt/ ZnIn_2S_4 nanostructures referring to previous photo-assisted electro-deposition method [27]. Certainly, the same three electrode configuration was used, with the resultant Pt/ ZnIn_2S_4 films acting as the working electrode. In this process, A bias of 0.4 V vs. Ag/AgCl electrode was applied to the working electrode for 60 s in the electrolyte with 0.1 M phosphate buffer (pH = 7) containing 0.5 mM cobalt nitrate under backside illumination of AM 1.5 simulated sunlight. After that, the as-prepared sample was swilled by alcohol and distilled water to remove the impurity ions staying on the surface of the sample and then dried in the air.

2.3. Characterization

The crystalline phases of the electrodes were examined by X-ray diffraction (XRD) using a Rigaku D/max-2500 with $\text{Cu K}\alpha$ radiation ($\lambda = 0.154059\text{ nm}$) at 40 kV and 200 mA. The surface chemical states and valence-band XPS spectra of the photocatalysts were recorded using X-ray photoelectron spectroscopy (Thermo ESCALAB 250Xi). Scanning electron microscope (SEM; JEOL JSM-7800 F) and transmission electron microscopy (TEM and HRTEM; JEOL JEM-2100) were performed for the morphological feature of samples. Concomitantly, the chemical composition and stoichiometry were implemented via an energy dispersive spectro-meter (EDS). The total surface area was calculated using Nova 3000e Surface Area Analyzers. Optical absorption measurements were carried out by a DU-8B UV-vis double-beam spectrophotometer (UV-vis absorption spectrometer). The photoluminescence (PL) spectra of the photocatalysts were recorded using a fluorescence spectrophotometer (FLS980, England).

2.4. Photoelectrochemical measurements

Photoelectrochemical tests were fulfilled through a three-electrode device, in which the resulting photoelectrodes were served as working electrode, also the reference and counter electrodes were kept the same as the above mentioned. A solar simulator (CHF-XM500, $100\text{ mW}\cdot\text{cm}^{-2}$) coupled with an air mass 1.5 G (AM 1.5 G) filter was used as the light source facing the back of the working electrode. 0.25 M Na_2SO_3 and 0.35 M Na_2S mixed solution was used as the electrolyte.

The measured potentials were converted to reversible hydrogen electrode (RHE) scale using the relationship:

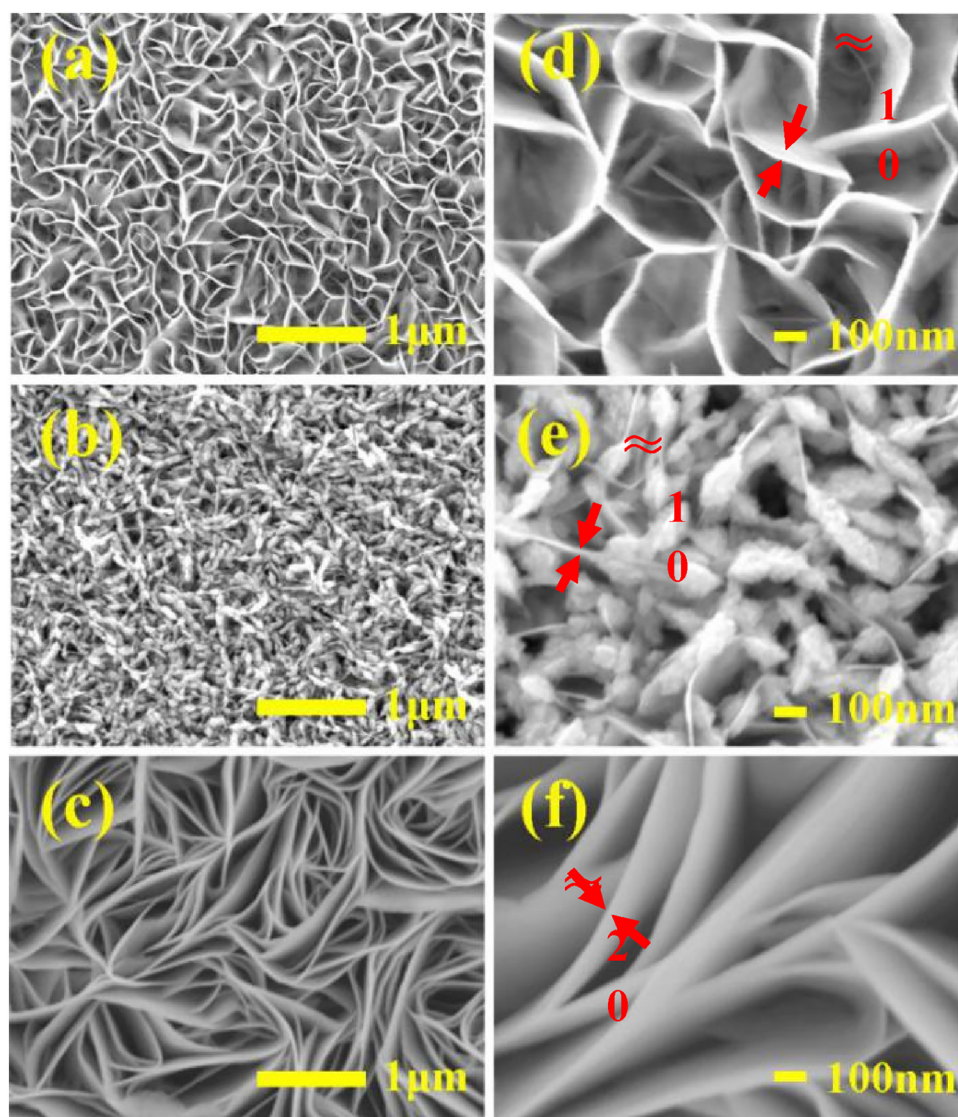


Fig. 1. SEM images of different ZnIn_2S_4 nanostructures via hydrothermal method with different precursor concentration: (a,d) ZIS-1, (b,e) ZIS-2, (c,f) ZIS-3.

$$E_{\text{RHE}} = E_{\text{Ag/AgCl}} + 0.0591 \times \text{pH} + E'_{\text{Ag/AgCl}} \quad (1)$$

where $E'_{\text{Ag/AgCl}}$ (saturated KCl) = 0.1976 V at 25 °C [28].

The incident photon to current efficiency (IPCE) was measured under monochromatic irradiation from Xe lamp equipped with band-pass filters. The IPCE at each wavelength was calculated with Eq [29]:

$$\text{IPCE} = (1240J)/(\lambda I_{\text{light}}) \times 100\% \quad (2)$$

In which λ corresponds to the incident light wavelength (nm), J is the photocurrent density ($\text{mA}\cdot\text{cm}^{-2}$) at wavelength λ under illumination, and I_{light} is the incident light irradiance intensity ($\text{mW}\cdot\text{cm}^{-2}$).

Electrochemical impedance spectroscopy (EIS) measurements were performed using a electrochemical workstation. EIS measurements were conducted at a frequency range of 10 Hz to 100 kHz with an amplitude of 10 mV under AM 1.5 G illumination. Mott-Schottky tests were performed at a frequency of 1000 Hz with AC amplitude of 10 mV.

3. Results and discussion

The morphological features of all samples with different precursor concentration were performed by SEM and the results are presented in Fig. 1. From the top view image (Fig. 1(a) and (d)) of the lowest precursor concentration (ZIS-1), we can clearly see that numerous

vertically oriented and interconnected nanoflakes (NFs) with thickness of about 10 nm uniformly grow in-situ on the substrate in large scale. And these thin nanoflakes interconnect to form a net-like porous microstructure. Furthermore, as can be illustrated in Fig. 1(b) and (e), when the concentration comes to a middle value (ZIS-2), there are amount of aggregate 0 dimension (0D) nanoparticles with the size of 100–300 nm randomly graft onto the 2 dimension (2D) nanoflakes in comparison to the lowest concentration. Similarly, the thickness of the 2D nanoflakes is also about 10 nm. In order to further prove the crystal structure of 0D nanoparticles, TEM characterization and the corresponding EDS mapping were conducted as shown in Fig. S1. It further confirms that the 0D nanoparticles, in which Zn, In and S are distributed homogeneously. The reason for this phenomenon is that there are not enough species to make distributed ZnIn_2S_4 nuclei grow into nanoflakes. Interestingly, we named this integrated morphological characteristic as edamame shaped ZnIn_2S_4 . Both Fig. 1(c) and (f) depicts the SEM image of ZnIn_2S_4 nanostructures obtained at high precursor concentration (ZIS-3). It can be found that the nanoplates (NPs) densely disperse in the space without any aggregation and the thickness of nanoplates is about 20 nm, which is thicker than NFs. Along with the increase of concentration, more nucleation centers cause so faster growth that nanoflake films are formed rapidly and the secondary growth occurs concomitantly. These results confirm that the precursor

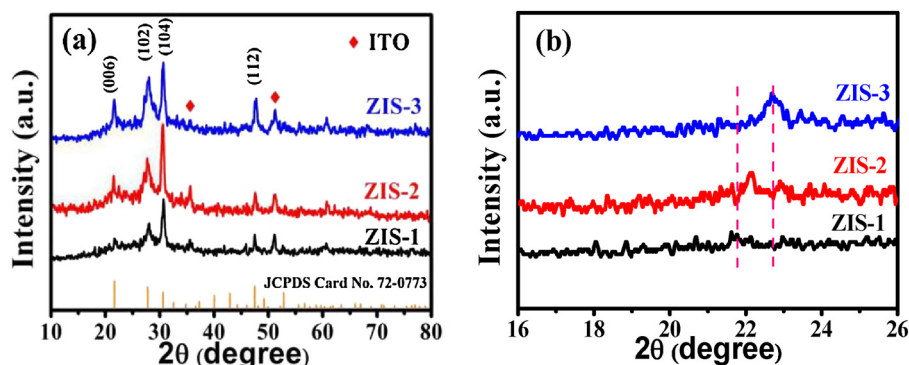


Fig. 2. XRD patterns of ZIS-1, ZIS-2 and ZIS-3.

concentration quite affects the final morphology of ZnIn_2S_4 nanostructures.

The crystallographic structure and phase composition of the resulting ZnIn_2S_4 nanostructures with different precursor concentration were confirmed by the X-ray diffraction (XRD) patterns as shown in Fig. 2. It can be obvious that the diffraction peaks of all products at 21.58° , 27.69° , 30.45° and 47.78° correspond to (006), (102), (104) and (112) planes of the hexagonal phase of ZnIn_2S_4 (JCPDS No. 72-0773) with the space group of $P6_3mc$ and the lattice parameters of $a = b = 3.85 \text{ \AA}$ and $c = 24.68 \text{ \AA}$. Except as the diffraction peaks of ZnIn_2S_4 , the other small peaks marked with the symbol “◆” in Fig. 2 are most likely due to the contribution of ITO substrate. Distinctly, there are no other diffraction peaks of impurities, including ZnS , In_2S_3 , oxides or organic complexes associated with the reactants, which reflects the phase purity of ZnIn_2S_4 . Additionally, all XRD patterns also manifest that the ZnIn_2S_4 products acquired via different precursor concentration are of high phase purity. Nevertheless, of particular note is that the position of peak (006) is shifted slightly to higher angle with the precursor concentration increasing, as shown in Fig. 2b, which results in the decreasing of d (006) space. This may be due to the more compact layered structure of the ZnIn_2S_4 products synthesized via a high precursor concentration, considering the ZnIn_2S_4 products possess a layered crystal structure as shown in Fig. 3a, in which the stacking of atoms along the c -axis is in a repeated sequence of S-Zn-S-In-S-In-S [30]. What's more, as we know, the d (006) space is consistent with one sixth of the lattice constant along the c -axis of the ZnIn_2S_4 structure. That is to say, precursor concentration could affect the crystal structure of ZnIn_2S_4 products prepared under the hydrothermal synthetic process, which is in accordance with the results of Fig. 1. The typical EDS spectrum is conducted to further examine the purity of the as-prepared ZnIn_2S_4 sample. As the quantitative composition analysis results present in Fig. 3b, the sample is consisted of Zn, In and S elements with the atomic ratio is about 1:2.01:4.02 as expected, which is in agreement with the standard stoichiometric ratio (1:2:4). Moreover, X-ray photoelectron

spectroscopy (XPS) was employed to examine the composition and chemical valence status of ZnIn_2S_4 nanostructure with different morphologies. From Fig. S2a, it can be clearly seen that the binding energies of $\text{Zn } 2p_{3/2}$ and $\text{Zn } 2p_{1/2}$ for ZnIn_2S_4 located at 1021.8 and 1044.8 eV are typical peaks for divalent zinc (Zn^{2+}) in a previous report [31]. The regional spectrum of $\text{In } 3d$ (Fig. S2b) shows a pair of symmetrical peaks with binding energies centred at 445.1 and 452.7 eV for $\text{In } 3d_{5/2}$ and $\text{In } 3d_{3/2}$ matching well with In (III) . The $\text{S } 2p$ core splits into two obvious peaks with binding energies at 161.8 eV for $\text{S } 2p_{3/2}$ and 163 eV for $\text{S } 2p_{1/2}$ [32], respectively. The results observed above indicated that the chemical valence states of the products are Zn^{2+} , In^{3+} and S^{2-} , confirming that there are not any chemical state change in ZIS-1, ZIS-2 and ZIS-3.

Based on the SEM and crystal structure observation, along with chemical composition analysis, it can be concluded that the uniform edamame shaped ZnIn_2S_4 film consisted of 0D NPs and 2D NFs was successfully synthesized via a facile hydrothermal route without any templates or additive, and in the absence of using any intricate process or expensive equipment. In principle, crystal structure, the surface and interfacial energies as well as the degree of the supersaturation account for crystal growth and crystal morphology. In this work, despite the detailed growth mechanism of edamame shaped ZnIn_2S_4 nanostructure is still not clear, the above results permit us to propose a possible process of obtained edamame shaped ZnIn_2S_4 nanostructure. Fig. 4 depicts the schematic illustration for the formation process of edamame shaped ZnIn_2S_4 nanostructure. In detail, after $\text{ZnCl}_2 \cdot 4\text{H}_2\text{O}$, $\text{InCl}_3 \cdot 4\text{H}_2\text{O}$ and TAA are dissolved in water, Zn^{2+} and In^{3+} ions diffuse slowly and are adsorbed on the surface of ITO under hydrothermal reaction conditions of high temperature and pressure, which enhances the ohmic contact between the conductive substrate and the deposited films [28]. Meanwhile, TAA not only works as a sulfur source, but also plays an important role in the formation of ZnIn_2S_4 nanostructure. The slow release and controlled supply of H_2S by the hydrolysis of TAA in the hydrothermal reaction was helpful to the nucleation and growth of

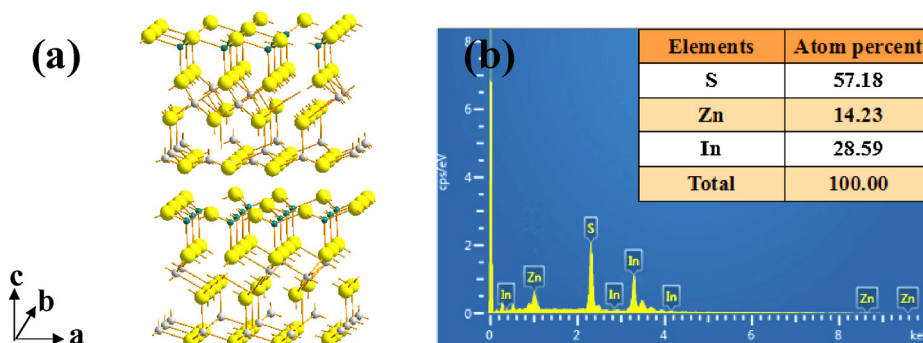


Fig. 3. (a) crystal structure of ZnIn_2S_4 , Zn, In, and S atoms are depicted in cyan, gray, and yellow balls, respectively and (b) EDS spectrums of ZnIn_2S_4 (For interpretation of the references to colour in this figure legend, the reader is referred to the web version of this article).

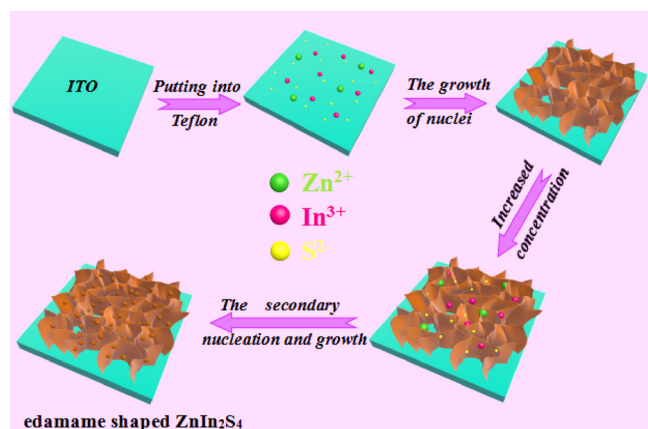
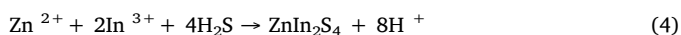


Fig. 4. A schematic illustration of the formation of the edamame shaped ZnIn_2S_4 .

ZnIn_2S_4 seeds on the ITO substrate [33]. The main reaction can be described as follows:



Along with the reaction continued, the secondary nucleation occurs preferentially on the ZnIn_2S_4 nuclei surface than those in the solution. Whereafter, based on these original particles, the evolved ZnIn_2S_4 nanoparticles are loaded onto the ZnIn_2S_4 nuclei consecutively, due to the lower concentration of the reactants around the growing crystals near the substrate. Subsequently, more and more thermodynamically unstable crystalline grains are ruined by the surrounding grains, and only those give priority to grow along the highest growth rate facets and perpendicular to the substrate can survive. These nanocrystals then continued to grow sideways result in the formation of interconnected nanoflakes on the ITO substrate. According to an intrinsic laminar structure of the hexagonal ZnIn_2S_4 phase, the formation of nanoflakes is believed to develop naturally under certain hydrothermal conditions, in which Zn and half of the In atoms are tetrahedrally coordinated by sulfur atoms, while the other half is an octahedral coordination. In the view of thermodynamics, the surface energy of a single nanoflakes with two main exposed planes is so high that they aggregate to the surface planes to decrease the surface energy through reducing exposed areas. Furthermore, reactant concentrations would induce the nucleation and crystal rate [34]. As the reactant concentration comes to a certain point, only a few ZnIn_2S_4 nuclei formed from the reactant solution result in not enough starting materials to enable the crystal nuclei to grow into more ZnIn_2S_4 nanoflakes. As a result, well-crystallized nanoflake films were formed, with some ZnIn_2S_4 nanoparticles covering the nanoflakes.

The optical performance of ZnIn_2S_4 films with different morphologies was characterized by UV–vis absorption spectra using the ITO substrate as the reference at room temperature. The absorption edge of the films is determined by the intersection of the tangent of sharply decreasing region and the baseline [35]. As shown in Fig. 5a, the spectrum indicates that the all ZnIn_2S_4 nanostructures present similar absorption edge in shape. However, note that the edamame shaped ZnIn_2S_4 nanostructure presents enhanced light absorption intensity and broader absorption region in visible light range with a strongly absorbed edge at about 500 nm, suggesting an optimal morphology of ZnIn_2S_4 structure. Such a phenomenon mainly can be attributed to the reason that the special morphology composed of hybrid 2D nanoflakes and 0D nanoparticles due to the same crystal structure of them. On the one hand, the interlaced nanoflakes can improve the light harvesting by multiple reflections between the nanoflakes. On the other hand, the

dispersive nanoparticles further boost the lighting scattering ability due to the rough surface, therefore, pretty more photons would be trapped and utilized [13]. Moreover, the band gaps of all samples are calculated based on the relationship between the band edge and optical absorption as shown in the inset of Fig. 5a. It can be clearly seen that the approximate band gap value of edamame shaped ZnIn_2S_4 is determined to be 2.48 eV, which is smaller than others (2.53 eV for ZIS-1, 2.51 eV for ZIS-3). Also, the values is consistent with the previously published dates [36], revealing availability of the method. According to the aforementioned analysis, the outstanding optical performance of ZnIn_2S_4 films can be ascribed to the factors of high light harvesting ability and narrow band gap. To the best knowledge of us, this light trapping effect may contribute to enhanced PEC performance in the process of water splitting. Besides, from Fig. 5a, it can be noticed that the transparent ITO turns to yellow, which demonstrates ZnIn_2S_4 film is coated on the ITO glass substrates successfully through hydrothermal process.

Subsequently, since the photocurrent density is the most direct and explicit characteristic of PEC performance, linear sweep voltammetry (LSV) curves of the resulting samples are measured in 0.25 M Na_2SO_3 and 0.35 M Na_2S electrolyte with a three-electrode configuration. In Fig. 5b, it is worth noting that all the samples display distinct photocurrent upon sweeping the potential from -0.2 to 1.4 V_{RHE} under illumination, which revealing efficient photo induced charge generation and separation at the interfaces of semiconductor/electrolyte. In this regard, the as prepared ZnIn_2S_4 NPs exhibit a photocurrent density of 0.29 mA/cm^2 at 1.23 V vs. RHE, which is higher than that of ZnIn_2S_4 NFs photoelectrode. Such phenomena may be attributed to the thicker nanosheets of ZnIn_2S_4 NPs that can enhance light capture and utilize for producing more charge for interfacial redox reactions, which is in line with the result of Fig. 5a. In the case of edamame shaped ZnIn_2S_4 , the photocurrent density is highest of all, which is up to 0.37 mA/cm^2 at 1.23 V vs. RHE. For the reason, on the one hand, the exist of nanoflakes increase the contact area with electrolyte, so as to improve the PEC properties. One the other hand, the coarse nanoparticles provide more active sites for redox reaction, which can be proved by BET surface areas measurement. With that, the total surface area was calculated using Nova 3000e Surface Area Analyzers. The surface area of ZnIn_2S_4 is with different morphologies as nanoflakes, edamame shaped nanostructure and nanoplates is 16.910 $\text{m}^2 \text{g}^{-1}$, 23.104 $\text{m}^2 \text{g}^{-1}$ and 18.021 $\text{m}^2 \text{g}^{-1}$, respectively, confirming that the more active sites were provided by edamame shaped ZnIn_2S_4 , which possesses the special component of coarse nanoparticles.

The design and synthesis of photoelectrodes with spatially charge-separated oxidation and reduction cocatalysts seem a promising and intriguing route to significantly improving the PEC conversion efficiency [37]. Accordingly, we firstly construct spatial charge separation layers (outer for Co-Pi and inner for Pt) on ZnIn_2S_4 nanostructures. Also, motivated by the above analysis, edamame shaped ZnIn_2S_4 have been chosen to be prototypes to clarify the enhanced PEC behavior. The typical top view and the magnified SEM images of Pt layer are displayed in Fig. S3. From them, we can see that Pt nanoparticles (NPs) is covered in the substrate absolutely and tightly with quiet small size of about 10 nm. Moreover, the thickness of Pt layer is too thinner to see from the inset of Fig. S3. Fig. 6a depicts the typical top view SEM image of Co-Pi/ ZnIn_2S_4 /Pt nanocomposite. There are no obvious change can be found in comparison with the SEM image of edamame shaped ZnIn_2S_4 , but sporadic floccule distribute on the surface of ZnIn_2S_4 , indicating bits of Co-Pi loaded on the surface of edamame shaped ZnIn_2S_4 . Concomitantly, it is too bushy edamame shaped ZnIn_2S_4 to see the existence of Pt NPs. Moreover, the thickness of Co-Pi/ ZnIn_2S_4 /Pt compounds is found to be 875 nm (Fig. 6b). The transmission electron microscopy (TEM) and high-resolution TEM (HRTEM) were employed to better understand the microstructure of Co-Pi/ ZnIn_2S_4 /Pt composite. The low-magnification TEM image (Fig. S4a) reveals that ZnIn_2S_4 connects with Pt NPs and amorphous Co-Pi. A high-resolution (HR)-TEM image reveals that the ZnIn_2S_4 sample is well crystallized, showing a clear lattice

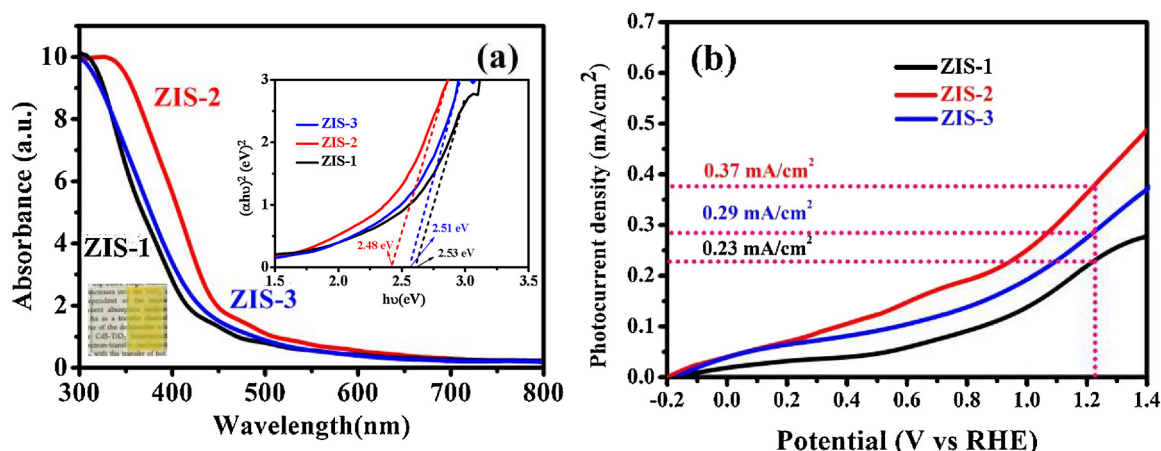


Fig. 5. (a) UV-vis absorption spectra and (inset) the plot of $(\alpha h\nu)^2$ versus $h\nu$ of all samples and (inset) photographs of ZnIn_2S_4 and blank indium-doped tin oxide (ITO) glass substrate and (b) linear sweep voltammetry (LSV) curves of all ZnIn_2S_4 samples.

with a spacing of 0.293 nm for the (104) lattice planes (Fig. S4b). While the Pt NPs, with a spacing of 0.198 nm consistent with the Pt (200) planes.

The XRD patterns of the resulting samples are shown in Fig. 7a. The indistinguishable XRD pattern of Co-Pi/ ZnIn_2S_4 with that of bare ZnIn_2S_4 due to the amorphous microstructure of the Co-Pi cocatalyst. Coincidentally, due to ultrathin Pt layer, the crystallinity of Pt is not good, there is only one weak peak corresponding to Pt NPs with the label of “★” in the pattern of Co-Pi/ ZnIn_2S_4 /Pt nanocomposites. Hence, to further confirm the existence of Co-Pi and Pt, elemental distribution mapping analysis under SEM observation was performed and is shown in Fig. 7b. Obviously, Zn, In, S, Pt, Co and P elements coexist in the Co-Pi/ ZnIn_2S_4 /Pt, manifesting Co-Pi/ ZnIn_2S_4 /Pt nanocomposite was synthesized successfully. XPS measurement was performed to further prove the successful deposition of Pt and CoPi cocatalysts on ZnIn_2S_4 . Fig. S5a and b shows the Co 2p, P 2p XPS scans at higher resolution over energy windows, respectively. The characteristic peaks of Co 2p_{3/2} and Co 2p_{1/2} at around 781.58 and 797.38 eV are in the typical range of Co²⁺ and Co³⁺, respectively.[47] The binding energy of P 2p is at ≈ 133.28 eV, which is the characteristic peak of P in the phosphate group. In addition, in the Pt 4f spectra (Fig. S5c), two peaks loaded at 71.1 and 74.5 eV could be assigned to metal Pt⁰. In conclusion, the results obtained above provide powerful evidence for the successful deposition of Pt and Co-Pi cocatalysts on ZnIn_2S_4 .

To explore the optical properties of Co-Pi/ ZnIn_2S_4 /Pt, ZnIn_2S_4 /Pt and Co-Pi/ ZnIn_2S_4 nanocomposites, the UV-vis absorption spectra is conducted in comparison to the pure ZnIn_2S_4 nanostructure (Fig. 8). Distinctly, the curve collected from Co-Pi/ ZnIn_2S_4 nanocomposites shows a similar light absorption edge to ZnIn_2S_4 , suggesting no supererogatory band gap transition caused by Co-Pi. Concomitant with this, the incident light may be consumed by Co-Pi layer via nonproductive

absorption[30], thus all the PEC experiments under light were executed with a backside illumination. What's more, there is no obvious red shift of absorption edge can be found after addition of Pt NPs underlayer on Co-Pi/ ZnIn_2S_4 . However, indeed, the light absorption intensity of Co-Pi/ ZnIn_2S_4 /Pt device is higher than the others, reflecting a strong light harvesting ability in the case of the present of a Pt NPs underlayer. We can see that Pt layer exhibits slight absorption intensity in Fig. S6. Also, from the photographs of ZnIn_2S_4 and Co-Pi/ ZnIn_2S_4 /Pt, it can be deduced that the Co-Pi/ ZnIn_2S_4 /Pt compound was fabricated successfully. There is no doubt that this promoted light capturing property of the structure is favorable for solar water splitting.

Then, linear sweep voltammetry (LSV) curves of all samples were collected in Fig. 9a using the above three electrode configuration to clarify the PEC performance of spatially separated cocatalysts (Co-Pi for outer and Pt for inner) on the edamame shaped ZnIn_2S_4 photoelectrode. Compared with the pristine one, the photocurrent density of Co-Pi/ ZnIn_2S_4 /Pt nanocomposite is significantly increased over the entire potential range from -0.4 to 1.4 V vs. RHE, which is up to 0.91 mA/cm² at 1.23 V vs. RHE. It is nearly 2.46 times higher than that of the bare one. The Pt/ ZnIn_2S_4 shows enhanced value of photocurrent density at 0.45 mA/cm² (1.23 V vs. RHE) due to the accelerated back electron injection and reduced interfacial recombination between the ZnIn_2S_4 and the ITO conductive substrate [38,39]. As for Co-Pi/ ZnIn_2S_4 , the photocurrent density is 0.53 mA/cm² at 1.23 V vs. RHE, which is improved through the whole potential range but still lower than that of Co-Pi/ ZnIn_2S_4 /Pt photoelectrode. To the best of our knowledge, a more negative photocurrent onset potential is significantly requisite for reducing the external bias needed for water oxidation reaction [40]. It is detected that Co-Pi/ ZnIn_2S_4 /Pt exhibits an evident negative shift of ~ 210 mV in the onset potential, implying the reduced surface state densities of the electrodes and the increased charge transfer rates at the

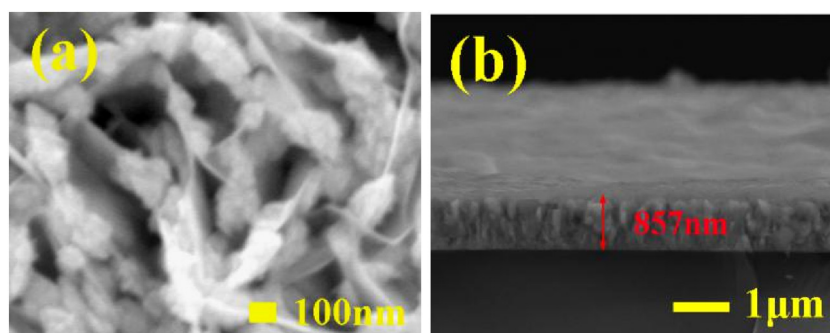


Fig. 6. (a) Typical top view SEM image of Co-Pi/ ZnIn_2S_4 /Pt compound and (b) the corresponding cross-section SEM image.

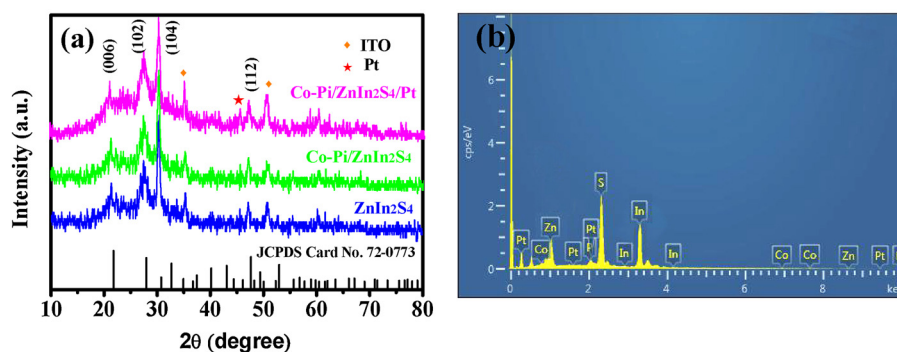


Fig. 7. (a) XRD patterns of edamame shaped ZnIn_2S_4 , $\text{Co-Pi/ZnIn}_2\text{S}_4$ and $\text{Co-Pi/ZnIn}_2\text{S}_4/\text{Pt}$ and (b) EDS spectrum collected for $\text{Co-Pi/ZnIn}_2\text{S}_4/\text{Pt}$.

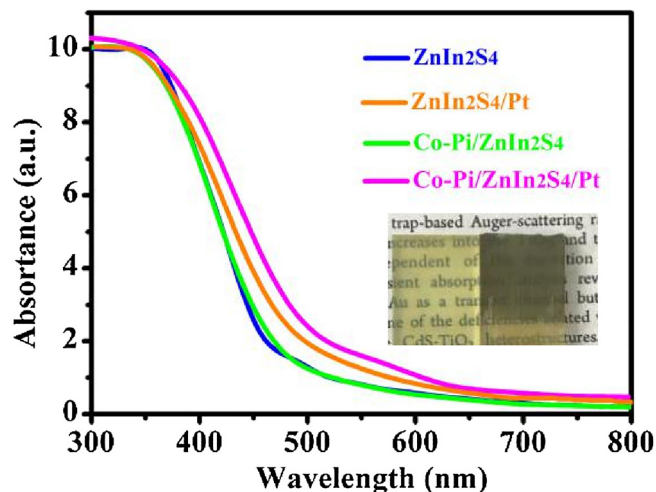


Fig. 8. UV-vis spectra of ZnIn_2S_4 , $\text{ZnIn}_2\text{S}_4/\text{Pt}$, $\text{Co-Pi/ZnIn}_2\text{S}_4$ and $\text{Co-Pi/ZnIn}_2\text{S}_4/\text{Pt}$ composite structure and (inset) photographs of ZnIn_2S_4 and $\text{Co-Pi/ZnIn}_2\text{S}_4/\text{Pt}$, respectively.

interface of $\text{Co-Pi/ZnIn}_2\text{S}_4$ [41]. Also, the photogenerated electrons can be trapped by Pt easily due to the Fermi level of Pt metal, which facilitates the separation and transport of charge carriers. This can be beneficial to the negative shift of photocurrent onset potential. The light photoresponse of all photoelectrodes is confirmed by photocurrent density – time (I-T) curves measurements at 1.23 V vs. RHE under chopped light irradiation as shown in Fig. 9b. It is noteworthy that the photocurrents of all samples show acutely rise up and drop down at the beginning and end of each chop, suggesting that the charge transportation in photoelectrodes is quite quickly. The photocurrent densities collected from the resulting ZnIn_2S_4 , $\text{Pt/ZnIn}_2\text{S}_4$, $\text{Co-Pi/ZnIn}_2\text{S}_4$, $\text{Co-Pi/ZnIn}_2\text{S}_4/\text{Pt}$ photoelectrodes are 0.36, 0.43, 0.51 and 0.89 mA/cm^2 , respectively, which are nearly agree with the photocurrent densities shown in Fig. 9a.

Following, to illustrate the relationship between applied voltage and photocurrent density, the applied bias photon-to-current efficiency (ABPE) was carried out as displayed in Fig. 9c. The values are calculated with the following Eq. (6) [42]:

$$\eta (\%) = I_{\text{PEC}} \cdot (V_{\text{redox}} - V_i) / P_{\text{light}} \cdot 100\% \quad (6)$$

where I_{PEC} , V_{redox} , V_i and P_{light} is the measured photocurrent density (mA/cm^2), the redox potential of electrochemical water splitting

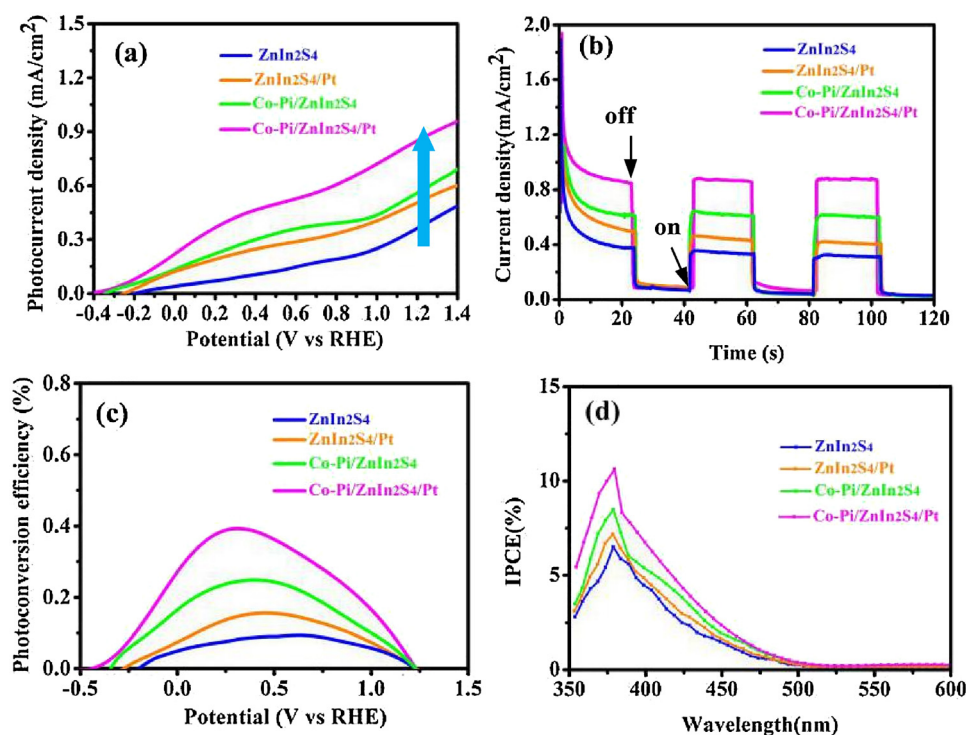


Fig. 9. Photoelectrochemical performance of ZnIn_2S_4 , $\text{ZnIn}_2\text{S}_4/\text{Pt}$, $\text{Co-Pi/ZnIn}_2\text{S}_4$ and $\text{Co-Pi/ZnIn}_2\text{S}_4/\text{Pt}$ photoanodes. (a) linear sweep voltammetry (LSV) curves; (b) Photocurrent density – time (I-T) curves; (c) the calculated applied bias photon-to-current efficiency (ABPEs) curves and (d) incident photon conversion efficiencies (IPCEs) plots.

(1.23 V), the applied external bias (V) and the incident illumination irradiance intensity (100 mW/cm^{-2} , AM 1.5 G), respectively.

As anticipated that the ABPE value of Co-Pi/ZnIn₂S₄/Pt photoelectrode is 0.39% at a low bias of 0.25 V vs. RHE, which is about 4.3 folds higher than the pure one (0.09% at 0.7 V vs. RHE). Such results can be ascribed to the decrease of hole and electron injection barrier at electrode/electrolyte interface induced by Co-Pi layer and electrode/ITO interface caused by Pt layer, respectively. Concomitant with this, the incident photo-to-current conversion efficiency (IPCE) measurements are conducted on the resultant samples under an applied bias of 1.23 V vs. RHE to quantify the contributions of monochromatic light to the photocurrent. In Fig. 9d, it can be found that introducing Co-Pi and Pt on the ZnIn₂S₄ photoanode leads to dramatically enhanced IPCE value throughout the entire spectral range from 350 to 600 nm in comparison with the single one and the maximum IPCE value of about 11% is obtained at 370 nm. The IPCE results verify that the ability of converting photogenerated holes to productive redox equivalents is promoted due to the existence of Co-Pi and Pt cocatalyst. Also, PL characterization is usually used to evaluate the charge separation efficiency for semiconductor photocatalyst. Thus, the charge separation efficiency of pure ZnIn₂S₄ and ZnIn₂S₄ loaded with different cocatalyst were measured and the results are displayed in Fig. S7. The PL intensity of pure ZnIn₂S₄ is the strongest, indicating the serious photogenerated charge recombination. The PL intensity decreases after introducing Co-Pi and/or Pt. Specially, Co-Pi/ZnIn₂S₄/Pt composite shows lower intensity by comparing with others, manifesting that the recombination rate of electrons and holes is inhibited considerably in Co-Pi/ZnIn₂S₄/Pt.

In order to further elucidate charge transfer and recombination process at Co-Pi and Pt modified ZnIn₂S₄, the electrochemical impedance spectroscopy (EIS) measurements are investigated as presented in Fig. 10. Generally known, the radius of the circle at high frequencies in a Nyquist plot means the charge transfer resistance (R_{ct}), that is, the smaller the radius is, the faster the charge transfer at the electrode-electrolyte interface is [43]. The ZnIn₂S₄ treated with Co-Pi and Pt NPs reflects smallest impedances than others, demonstrating improved charge transport speed and decreased charge recombination produced by the synergistic effect between Co-Pi and Pt, which confirms the above explanation for the excellent PEC performances. In addition, photostability of photoelectrode is a significant criterion for practical applications of the PEC cell. Thus, the stability of the synthesized Co-Pi/ZnIn₂S₄/Pt photoanode is studied under 1 h simulated sunlight illumination. As suggested by Fig. S8, the photocurrent of Co-Pi/ZnIn₂S₄/Pt electrode decays to a stable level of about 0.7 mA/cm^2 and then keeps at a relative stable level.

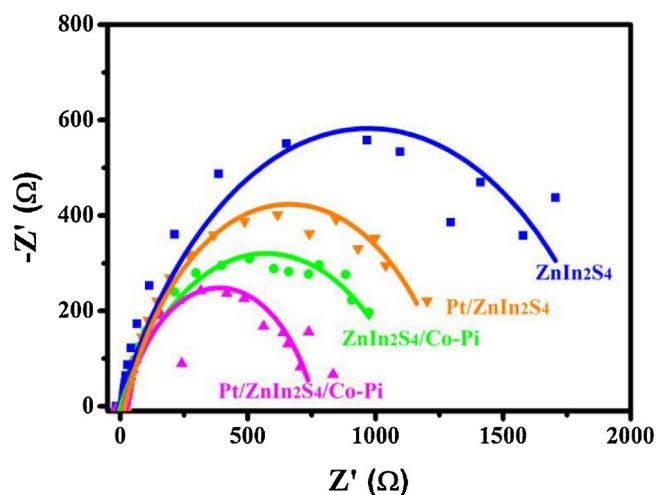


Fig. 10. Electrochemical impedance spectroscopy (EIS) for ZnIn₂S₄, ZnIn₂S₄/Pt, Co-Pi/ZnIn₂S₄ and Co-Pi/ZnIn₂S₄/Pt.

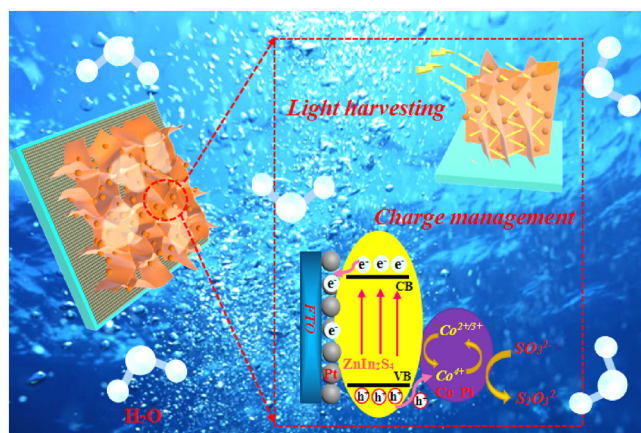


Fig. 11. Charge transfer mechanism and photoelectrochemical activity of Co-Pi/ZnIn₂S₄/Pt photoanode.

Based on the aforementioned characterization analyses and experimental results, a convincing mechanism illustrating the enhanced PEC behaviors of the Co-Pi/ZnIn₂S₄ nanocomposites is illustrated in Fig. 11. First of all, light absorption is the cornerstone of the PEC water splitting, edamame shaped ZnIn₂S₄ nanostructure can increase photon-matter interaction via multiple reflection and scattering at the semiconductor surface, which can be enhanced by rough (0D) NPs covering the surface of (2D) NFs. Meanwhile, a considerable number of electron-hole pairs can be excited. Also, the photogenerated holes are driven to Co-Pi nanoparticles to occur circular catalytic $\text{Co}^{2+/3+} \rightarrow \text{Co}^{4+} \rightarrow \text{Co}^{2+/3+}$ reactions [40], which suppresses the recombination of the photo-generated carriers and prolongs its lifetime, thereby, significantly promoting the PEC performance of H₂ generation. Meanwhile, the Pt layer shows higher electron capture capability located in the interface of the semiconductor/conductor due to the decreased charge-transfer barriers by benign Fermi level of Pt, facilitating the photo-induced electron transfer to the substrate. Thereby, electrons will flow to counter electrode via the external circuit to produce H₂. Hence, the combined effect of spatially separated Co-Pi and Pt NPs fully optimize the separation and transfer of photoexcited electron-hole pairs. In brief, the synergistic enhancement of Light harvesting and charge management by sandwiched with Co-Pi/ZnIn₂S₄/Pt Structures thus result in increased PEC performance.

4. Conclusion

In summary, we have designed a novel edamame shaped ZnIn₂S₄ nanostructures consisted of hybridized nanoflakes (2D) and nanoparticles (0D) on ITO conductive substrate through a simple hydrothermal method for PEC water splitting for the first time. The growth mechanism of ZnIn₂S₄ is discussed in detail. The series of PEC measurements indicate that edamame shaped ZnIn₂S₄ films exhibit relatively higher PEC activity (0.37 mA/cm^2 at 1.23 V vs. RHE) than that of ZnIn₂S₄ NFs and ZnIn₂S₄ NPs due to the enhanced light absorption and efficient charge separation and transfer by reduced transmission distance of photogenerated carriers and increased active sites. Additionally, after selectively depositing Co-Pi cocatalyst and Pt NPs on the top and bottom sides of edamame shaped ZnIn₂S₄ photoanodes, charge recombination at the surface and interface can be efficiently reduced. The spatial Co-Pi cocatalyst drives holes to flow to the surface, while the Pt NPs facilitate the electrons in the opposite directions. Thus, the integrated Co-Pi/ZnIn₂S₄/Pt equipment without any additional doping presents an increased photocurrent density with 0.91 mA/cm^2 at 1.23 V vs. RHE. This work highlights that edamame shaped ZnIn₂S₄ can be a promising candidate for photoelectrochemical behavior and route such as coupling of Co-Pi and Pt co-catalysts on photoanodes have

an interfacial electric field can provide a new avenues to design efficient PEC devices in future.

Acknowledgements

The authors gratefully acknowledge financial support from Science Funds of Tianjin for Distinguished Young Scholar (No. 17JCJQJC44800) and Natural Science Foundation of Tianjin (No. 16JCYBJC17900).

Appendix A. Supplementary data

Supplementary material related to this article can be found, in the online version, at doi:<https://doi.org/10.1016/j.apcatb.2018.11.031>.

References

- [1] M.G. Walter, E.L. Warren, J.R. McKone, S.W. Boettcher, Q. Mi, E.A. Santori, N.S. Lewis, Solar water splitting cells, *Chem. Rev.* 110 (2010) 6446–6473.
- [2] N.S. Lewis, Toward cost-effective solar energy use, *Science* 315 (2007) 798–801.
- [3] S. Dahl, I. Chorkendorff, Solar-fuel generation: towards practical implementation, *Nat. Mater.* 11 (2012) 100–101.
- [4] A. Fujishima, K. Honda, Electrochemical photolysis of water at a semiconductor electrode, *Nature* 238 (1972) 37–38.
- [5] G. Hodes, D. Cahen, J. Manassen, Tungsten trioxide as a photoanode for a photoelectrochemical cell (PEC), *Nature* 260 (1976) 312–313.
- [6] F.E. Osterloh, Inorganic nanostructures for photoelectrochemical and photocatalytic water splitting, *Chem. Soc. Rev.* 42 (2013) 2294–2320.
- [7] J.R. Bolton, S.J. Strickler, J.S. Connolly, Limiting and realizable efficiencies of solar photolysis of water, *Nature* 316 (1985) 495–500.
- [8] O. Khaselev, J.A. Turner, A monolithic photovoltaic-photoelectrochemical device for hydrogen production via water splitting, *Science* 280 (1998) 425–427.
- [9] J.E. Katz, T.R. Gingrich, E.A. Santori, N.S. Lewis, Combinatorial synthesis and high-throughput photopotential and photocurrent screening of mixed-metal oxides for photoelectrochemical water splitting, *Energy Environ. Sci.* 2 (2009) 103–112.
- [10] Z. Liu, X. Wang, Q. Cai, C. Ma, Z. Tong, CaBi_2O_6 : a novel promising photoanode for photoelectrochemical water oxidation, *J. Mater. Chem. A* 5 (2017) 8545–8554.
- [11] Q. Wang, J. He, Y. Shi, S. Zhang, T. Niu, H. She, Y. Bi, Z. Lei, Synthesis of MFe_2O_4 ($\text{M}=\text{Ni}, \text{Co}$)/ BiVO_4 film for photoelectrochemical hydrogen production activity, *Appl. Catal. B* 214 (2017) 158–167.
- [12] M. Zhou, Z. Liu, X. Li, Z. Liu, Promising three-dimensional flowerlike CuWO_4 photoanode modified with CdS and FeOOH for efficient photoelectrochemical water splitting, *Ind. Eng. Chem. Res.* 57 (2018) 6210–6217.
- [13] T. Hong, Z. Liu, J. Zhang, G. Li, J. Liu, X. Zhang, S. Lin, Flower-like $\text{Cu}_2\text{In}_2\text{ZnS}_5$ nanosheets: a novel promising photoelectrode for water splitting, *ChemCatChem* 8 (2016) 1288–1292.
- [14] Y. Lin, S. Zhou, X. Liu, S. Sheehan, D. Wang, $\text{TiO}_2/\text{TiSi}_2$ heterostructures for high-efficiency photoelectrochemical H_2O splitting, *J. Am. Chem. Soc.* 131 (2009) 2772–2773.
- [15] X.F. Wu, Y. Sun, H. Li, Y.J. Wang, C.X. Zhang, J.R. Zhang, J.Z. Su, Y.W. Wang, Y. Zhang, C. Wang, M. Zhang, In-situ synthesis of novel pn heterojunction of $\text{Ag}_2\text{CrO}_4\text{-Bi}_2\text{Sn}_2\text{O}_7$ hybrids for visible-light-driven photocatalysis, *J. Alloys. Compd.* 740 (2018) 1197–1203.
- [16] J. Zhang, H.P. Ma, Z. Liu, Highly efficient photocatalyst based on all oxides $\text{WO}_3/\text{Cu}_2\text{O}$ heterojunction for photoelectrochemical water splitting, *Appl. Catal. B* 201 (2017) 84–91.
- [17] Q. Yu, X. Meng, T. Wang, P. Li, J. Ye, Hematite films decorated with nanostructured ferric oxyhydroxide as photoanodes for efficient and stable photoelectrochemical water splitting, *Adv. Funct. Mater.* 25 (2015) 2686–2692.
- [18] L. Wang, N.T. Nguyen, Y.J. Zhang, Y.P. Bi, P. Schmuki, Enhanced solar water splitting by swift charge separation in Au/FeOOH sandwiched single crystalline Fe_2O_3 nanoflake photoelectrodes, *ChemSusChem* 10 (2017) 2720–2727.
- [19] D. Wang, T. Hisatomi, T. Takata, C. Pan, M. Katayama, J. Kubota, K. Domen, Core/Shell photocatalyst with spatially separated co-catalysts for efficient reduction and oxidation of water, *Angew. Chemie Int. Ed.* 52 (2013) 11252–11256.
- [20] A. Li, X. Chang, Z. Huang, C. Li, Y. Wei, L. Zhang, T. Wang, J. Gong, Thin heterojunctions and spatially separated cocatalysts to simultaneously reduce bulk and surface recombination in photocatalysts, *Angew. Chemie Int. Ed.* 55 (2016) 13734–13738.
- [21] J. Zhang, Z. Yu, Z. Gao, H. Ge, S. Zhao, C. Chen, Z.F. Zheng, Y. Qin, Porous TiO_2 nanotubes with spatially separated platinum and CoO_x cocatalysts produced by atomic layer deposition for photocatalytic hydrogen production, *Angew. Chemie Int. Ed.* 56 (2017) 816–820.
- [22] W.S. Seo, R. Otsuka, H. Okuno, M. Ohta, K. Koumoto, Thermoelectric properties of sintered polycrystalline ZnIn_2S_4 , *J. Mater. Res.* 14 (1999) 4176–4181.
- [23] S. Peng, L. Li, Y. Wu, L. Jia, L. Tian, M. Srinivasan, Q. Yan, S.G. Mhaisalkar, Size- and shape-controlled synthesis of ZnIn_2S_4 nanocrystals with high photocatalytic performance, *CrystEngComm* 15 (2013) 1922–1930.
- [24] W. Yang, L. Zhang, J. Xie, X. Zhang, Q. Liu, T. Yao, Q. Zhang, Y. Xie, Enhanced photoexcited carrier separation in oxygen-doped ZnIn_2S_4 nanosheets for hydrogen evolution, *Angew. Chemie Int. Ed.* 55 (2016) 6716–6720.
- [25] B. Gao, L. Liu, J. Liu, F. Yang, Photocatalytic degradation of 2, 4, 6-tribromophenol on Fe_2O_3 or FeOOH doped ZnIn_2S_4 heterostructure: insight into degradation mechanism, *Appl. Catal. B* 147 (2014) 929–939.
- [26] Z. Lei, W. You, M. Liu, G. Zhou, T. Takata, M. Hara, K. Domen, C. Li, Photocatalytic water reduction under visible light on a novel ZnIn_2S_4 catalyst synthesized by hydrothermal method, *Chem. Commun.* 17 (2003) 2142–2143.
- [27] G. Ai, R. Mo, H. Li, J. Zhong, Cobalt phosphate modified TiO_2 nanowire arrays as co-catalysts for solar water splitting, *Nanoscale* 7 (2015) 6722–6728.
- [28] M. Li, X. Tu, Y. Su, J. Lu, J. Hu, B. Cai, Z. Zhou, Z. Yang, Y. Zhang, Controlled growth of vertically aligned ultrathin In_2S_3 nanosheet arrays for photoelectrochemical water splitting, *Nanoscale* 10 (2018) 1153–1161.
- [29] Y. Yuan, J. Gu, K.H. Ye, Z.S. Chai, X. Yu, X.B. Chen, C.X. Zhao, Y.M. Zhang, W.J. Mai, Combining bulk/surface engineering of hematite to synergistically improve its photoelectrochemical water splitting performance, *ACS Appl. Mater. Interfaces* 8 (2016) 16071–16077.
- [30] F.G. Donika, S.I. Radautsan, G.A. Kiosse, S.A. Semiletov, T.V. Donika, I.G. Mustya, Crystal structure of the two-packet polytype ZnIn_2S_4 (II) a and refinement of the structure of the three-packet ZnIn_2S_4 (III) a, *Sov. Phys. Crystallogr.* 16 (1971) 235–241.
- [31] X. Tu, J. Lu, M. Li, Y. Su, G. Yin, D. He, Hierarchically ZnIn_2S_4 nanosheet-constructed microwave arrays: template-free synthesis and excellent photocatalytic performances, *Nanoscale* 10 (2018) 4735–4744.
- [32] B. Liu, H.C. Zeng, Fabrication of ZnO “dandelions” via a modified Kirkendall process, *J. Am. Chem. Soc.* 126 (2004) 16744–16746.
- [33] J.Q. Hu, B. Deng, W.X. Zhang, K.B. Tang, Y.T. Qian, Synthesis and characterization of CdIn_2S_4 nanorods by converting CdS nanorods via the hydrothermal route, *Inorg. Chem.* 40 (2001) 3130–3133.
- [34] J. Wang, P.S. Lee, J. Ma, One-pot synthesis of hierarchically assembled tungsten oxide (hydrates) nano/microstructures by a crystal-seed-assisted hydrothermal process, *Cryst. Growth Des.* 9 (2009) 2293–2299.
- [35] T.L. Li, Y.L. Lee, H. Teng, CuInS_2 quantum dots coated with CdS as high-performance sensitizers for TiO_2 electrodes in photoelectrochemical cells, *J. Mater. Chem.* 21 (2011) 5089–5098.
- [36] K.W. Cheng, C.J. Liang, Preparation of Zn-In-S film electrodes using chemical bath deposition for photoelectrochemical applications, *Sol. Energy Mater. Sol. Cells* 94 (2010) 1137–1145.
- [37] L. Wang, Y. Yang, Y. Zhang, Q. Rui, B. Zhang, Z. Shen, Y. Bi, One-dimensional hematite photoanodes with spatially separated Pt and FeOOH nanolayers for efficient solar water splitting, *J. Mater. Chem. A* 5 (2017) 17056–17063.
- [38] S.R. Pendlebury, A.J. Cowan, M. Barroso, K. Sivula, J. Ye, M. Grätzel, D.R. Klug, J. Tang, J.R. Durrant, Correlating long-lived photogenerated hole populations with photocurrent densities in hematite water oxidation photoanodes, *Energy Environ. Sci.* 5 (2012) 6304–6312.
- [39] L. Steier, I. Herraiz-Cardona, S. Gimenez, F. Fabregat-Santiago, J.S. Bisquert, D. Tilley, M. Grätzel, Understanding the role of underlayers and overlayers in thin film hematite photoanodes, *Adv. Funct. Mater.* 24 (2014) 7681–7688.
- [40] G. Ai, H. Li, S. Liu, R. Mo, J. Zhong, Solar water splitting by $\text{TiO}_2/\text{CdS}/\text{Co-Pi}$ nanowire array photoanode enhanced with Co-Pi as hole transfer relay and CdS as light absorber, *Adv. Funct. Mater.* 25 (2015) 5706–5713.
- [41] Y.X. Yu, W.X. Ouyang, Z.T. Liao, B.B. Du, W.D. Zhang, Construction of $\text{ZnO}/\text{ZnS}/\text{CdS}/\text{CuInS}_2$ core-shell nanowire arrays via ion exchange: p-n junction photoanode with enhanced photoelectrochemical activity under visible light, *ACS Appl. Mater. Interfaces* 6 (2014) 8467–8474.
- [42] J. Li, N. Wu, Semiconductor-based photocatalysts and photoelectrochemical cells for solar fuel generation: a review, *Catal. Sci. Technol.* 5 (2015) 1360–1384.
- [43] F. Nan, Z. Kang, J. Wang, M. Shen, L. Fang, Carbon quantum dots coated BiVO_4 inverse opals for enhanced photoelectrochemical hydrogen generation, *Appl. Phys. Lett.* 106 (2015) 153901–153905.